Supporting Information

Ma *et al.* 10.1073/pnas.0805501105

SI Text

Protein Expression and Sample Preparation. The published expression and purification procedures (1) were modified to increase the yield and to control aggregation of the purified WSK3. The yield was increased by approximately tenfold to ≈200 mg/liter by using the Marley protocol and growth at 15 °C (2). After growth at 37 °C in LB media containing 10 μg/ml kanamycin to an OD_{600} of 0.6, the culture was concentrated fourfold into M9 media with ^{15}N-$(NH_4)_2SO_4$ and 1% glucose for ^{15}N-labeled WSK3, or ^{15}N-$(NH_4)_2SO_4$ and 0.4% ^{13}C-glucose for ^{15}N,^{13}C-labeled WSK3. Because reasonable spectral resolution could be achieved with ^{15}N- or ^{15}N,^{13}C-labeled samples, deuterium labeling was not attempted. The cultures were grown at 15 °C for 2 h before induction with 1 mM IPTG. Induction was continued for 5 days at 15 °C. Cells were lysed by sonication, and the soluble extract, obtained after centrifugation at 370 kg for 30 min, was immediately subjected to ion-exchange chromatography using 50 ml Q-Sepharose Fast Flow (GE Healthcare) resin. The WSK3 eluting with 350 mM KCl was essentially pure, but produced poor NMR spectra because of higher-order soluble aggregation (as determined by size-exclusion chromatography). To prepare tetramer samples, WSK3 was diluted to <0.4 mg/ml in 0.1% trifluoroacetic acid (TFA, used as a counter ion), and reverse-phase chromatography was performed by using a C4 column. WSK3 was eluted with about 50% acetonitrile in 0.1% TFA, and acetonitrile was then completely removed by evaporation under a stream of nitrogen gas. The resultant solution was further diluted tenfold with water before lyophilization. The lyophilized samples were then dissolved in 95% H_2O and 5% D_2O. The pH was measured at 4.5 by using an Orion 98–63 microelectrode (Thermo Electron). For measuring the effects of ionic strength, KCl or NaCl solution was titrated directly into the NMR tubes.

Dynamic Light Scattering (DLS). DLS was performed by using a DynaPro plate reader and analyzed with Dynamics software (Wyatt Technology). Aliquots of NMR samples, taken directly from the NMR tubes without dilution and with stepped dilution, were measured. The scattering data were processed by using the regularization analysis protocol in the Dynamics software. Representative WSK3 autocorrelation graph and regularization plots for radius and diffusion coefficient distributions are shown in Fig. S1. The dominating population has a diffusion coefficient of 5.1×10^{-11} m^2/s and a hydrodynamic radius of ≈52 Å.

Circular Dichroism (CD). CD analysis was performed by using a Jasco Model J-810 spectrophotometer and analyzed by using the CDSSTR algorithm at the DICHROWEB server (3, 4). The far-UV CD spectrum of WSK3 was measured at a concentration of 26 μg/ml. A CD spectrum of WSK3 is depicted in Fig. S3, showing a highly helical structure.

Details of NMR Experiments. NMR measurements were recorded on Bruker Avance 600, 700, and 800 MHz spectrometers with Topspin 1.3 software (Bruker Instruments). All spectrometers were equipped with cryogenic triple-resonance probes with *z* axis pulsed field gradients. NMR pulse sequences from the Topspin sequence library, including HNCO, HNCA, HNCACB, and CBCACONH for sequential assignment, HCCH-TOCSY for side chain assignment, 3D ^{15}N- and ^{13}C-filtered or -edited NOESY for distance constraints, TROSY-IPAP for residual dipole coupling (5, 6), HSQC-based R_1 and R_2 sequences for ^{15}N relaxation parameters, HSQC-based CPMG method for R_2 dispersion measurements, and DOSY for the determination of the translational diffusion constant, were used without modification or with only minor modifications. Triple-resonance experiments were acquired typically with complex time domain size of 1024 (direct observation dimension) × 32–80 (filter dimension) × 256 (indirect observation dimension). The mixing times were 60 ms and 120 ms for ^{15}N-edited NOESY and 150 ms for ^{13}C-edited NOESY. The intersubunit NOE connectivity was determined by using a ^{13}C-edited, $^{13}C/^{15}N$-filtered 3D NOESY pulse sequence and a mixture of 1:1 molar ratio of $^{13}C/^{15}N$-uniform labeled and unlabeled WSK3. For RDC measurements, an anisotropic sample was prepared by using stretched 5% uncharged acrylamide gel following a published method (7). RDC data were acquired with 2,048 × 512 complex data points to ensure accurate measurements of resonance frequencies. Longitudinal and transverse relaxation rate constants, R_1 and R_2, and the steady-state ^{15}N-[^1H] NOE of the backbone amide ^{15}N were measured at 14.1 and 16.5 T by using 4-, 2.5-, and 3-s relaxation delays, respectively. R_1 was recorded by using 11 delay values: 0.01, 0.1, 0.2, 0.3, 0.5, 0.7, 1.0, 1.5, 2.0, 3.0, and 5.0 s. R_2 was recorded by using 12 delay values: 0.016, 0.032, 0.064, 0.096, 0.128, 0.160, 0.192, 0.256, 0.320, 0.480, 0.768, and 1.280 s. The steady-state ^{15}N-[^1H] NOE was measured with and without ^1H saturation in an interleaved fashion. Proton saturation was achieved by using a train of 120° high-power pulses separated by 5 ms for the duration of 3 s. The R_2 dispersion measurements were carried out at 16.5 T and 10 °C by using the relaxation-compensated, constant-time, Carr–Purcell–Meiboom–Gill (CPMG) sequence (8, 9) with the following 10 CPMG field strengths (ν_{CPMG}): 33.33, 66.67, 100.00, 133.33, 200.00, 266.67, 333.33, 400.00, 500.00, and 666.67 Hz. The reference spectrum was acquired without the CPMG period. A relaxation delay of 2.5 s was used.

NMR Data Processing and Analyses. NMRPipe (10) and Topspin were used to process all NMR data. Autoassign (11) and Sparky (12) were used to aid the resonance assignments. Backbone angles were predicted from chemical shifts by using the semiempirical method implemented in TALOS (13) in the NMRPipe software package.

The 3D structure was determined by using backbone angular constraints derived from chemical shifts and distance constraints obtained from 3D ^{15}N- and ^{13}C-filtered and -edited NOESY data, as well as the hydrogen bonding restraints and N-H residual dipolar coupling restraints for residues where these constraints were accurately measured. Initial NOE cross-peak assignments and structure calculations were carried out by using CYANA 2.1 (14, 15). An in-house script was used to assist the NOE assignments manually by matching the unassigned NOE peaks from the CYANA output with the resonance assignment table. As a standard protocol, NOE assignments and structure calculations were iterated such that the calculated preliminary structures were used to correct restraint violations and to reduce assignment ambiguities until a self-consistent solution to the entire dataset was obtained. Xplor-NIH (16) was then used to calculate and refine the structures with and without the RDC restraints. In this process, additional long-range distance restraints were assigned manually on the basis of the structures calculated in the previous iteration step. The refined structures were analyzed by using MOLMOL (17) and Procheck-NMR (18). Structural statistics are given in Table S1.

The likely formation of several intra- and intersubunit salt bridges has been revealed by the analyses of the refined solution structure of WSK3. Tables S2 and S3 list the key NOE distance constraints in support of the conclusions. Examples of NOE cross-peaks from different regions in the protein are given in Fig. S5 to illustrate the quality of the 3D NOESY spectra used for generating the distance restraints. More complete residue pairing for the 415 long-range NOE constraints is depicted in Fig. S6*C*.

NMR Diffusion Measurements. To determine the dominating oligomerization state of the protein contributing to the observed NMR signals, translational diffusion coefficients were measured by using diffusion-weighted NMR spectroscopy for the very same NMR samples used for the structure determination. Based on the Stokes law and the Sutherland–Einstein relationship between the diffusion coefficient and the frictional coefficient, a hydrodynamic radius, R_H, can be estimated by using $R_H = k_B T/6\pi\eta D F_p$, where k_B is the Boltzmann constant, T the absolute temperature, η the viscosity, D the diffusion coefficient, and F_p the Perrin shape correction factor (19, 20). Fig. S2 depicts the DOSY spectra of WSK3 and water at 30 °C. Only a single diffusion coefficient is associated with the protein peaks. The measured diffusion coefficients are $(2.1 \pm 0.2) \times 10^{-9}$ m^2/s for H_2O and $(5.8 \pm 0.6) \times 10^{-11}$ m^2/s for WSK3. The latter is in excellent agreement with the major population in the distribution determined by DLS. The estimated F_p values for water and for the WSK3 monomer and tetramer are 1.00, 1.09, and 1.00, respectively. By using water diffusion as an internal reference, it can be concluded that the effective hydrodynamic radius of the diffusing WSK3 particle is 49–51 Å, corresponding to a hydrodynamic molecular volume of $(4.9 \pm 1.2) \times 10^5$Å^3 for a monomer of cylindrical symmetry or $(5.4 \pm 1.3) \times 10^5$Å^3 for a tetramer of cylindrical symmetry after accounting as usual for hydration (21–24).

Analyses of WSK3 Chemical Shifts. The C_α chemical shift is predictive of the backbone torsion angle and, hence, the secondary structure. It is thus of interest to compare the chemical shifts of WSK3 in this study with the corresponding values of KcsA in the literature (25). Despite the very different sample conditions for the KcsA and WSK3 NMR measurements (50 °C in detergent micelles for KcsA versus 20 °C in water for WSK3), the C_α chemical shifts of the corresponding residues in the two proteins are quite similar. Fig. S4 shows C_α chemical shift correlations between WSK3 and KcsA. Similarly strong correlations also exist for the backbone N and C′. Although the correlation between backbone amide proton (HN) chemical shifts of the two proteins is not as strong, the HN chemical shift range for WSK3 and KcsA is similar. Most of the WSK3 HN resonances are concentrated between 7.82 and 8.45 ppm, yielding a 0.63-ppm spread. Most of the KcsA HN peaks clustered between 7.60 and 8.25 ppm, yielding a 0.65-ppm spread. Despite the narrow range, both KcsA and WSK3 are largely helical, as confirmed by the CD data.

Analyses of WSK3 Dynamics. The ^{15}N relaxation parameters and ^{15}N-{^{1}H} NOE were analyzed qualitatively by using the reduced spectral density mapping method (26, 27) and quantitatively by using the extended model-free approach (28). A ^{15}N-^{1}H internuclear bond distance of 1.02 Å and an ^{15}N chemical shift anisotropy of 172 ppm were used, in agreement with the NMR dynamics analysis of KcsA (29). Together, these values account for bond librations prevailing in the solid states (30, 31). The experimental R_2/R_1 ratios, and the J (0), $J(\omega_N)$, and $J(0.87\omega_H)$ values (with ω_N and ω_H denoting the ^{15}N and ^{1}H Larmor angular velocities) obtained from the reduced spectral density mapping analysis (27) of the data shown in Fig. 4 *A*–*C*, are depicted in Fig. S9. In agreement with the ^{15}N R_1 and R_2 profile, the R_2/R_1 ratios and $J(0)$ values are low and highly heterogeneous, and the $J(0.87\omega_H)$ values are high, as compared with typical globular protein values. Assuming isotropic global diffusion, the estimates for the global correlation time, τ_m, are 5.3 ns from R_2/R_1 ratio (32) and 3.8 ns from $J(0)$ (33). Clearly, these estimates are inadequate for a ≈45-kDa tetramer at 20 °C, be it spherical or of lower symmetry. Exchange domination of R_2 or $J(0)$ has been ruled out experimentally (no τ_{cp}-dependence of CPMG) and by the field-dependence of R_2 or $J(0)$, both of which are larger at 14.1 T than at 16.5 T, whereas the opposite trend would be expected from the ω^2 dependence of fast conformational exchange contributions (34). Thus, the unusual values of the experimental relaxation parameters must be related to complex dynamics, notably nanosecond slow motions, affecting the entire WSK3 backbone. In this case, the R_2/R_1-based (or $J(0)$-based) determination of the global diffusion tensor is no longer appropriate, and other means must be used.

As discussed in the main text, multiple lines of experimental evidence suggest tetramer prevalence in the WSK3 sample. Chill *et al.* (29) studied the detergent-solubilized KcsA tetramer with ^{15}N spin relaxation methods; the global correlation time, τ_m, was set to 38 ± 2.5 ns at 50 °C. Scaling this number by 45.5/120 (the denominator corresponds to the average molecular mass of the KcsA/detergent aggregates) and further by 1.2 [corresponding to a typical 1.2-fold increase in τ_m per 10 °C temperature decrease (35)] leads to 25 ns at 20 °C. This agrees with τ_m of ≈23 ns for a sphere having a molecular mass of 45.5 kDa.

In the model-free approach, the global motion of the protein, τ_m, and the effective local motion of the observed probe, τ_e, are assumed to be decoupled because $\tau_e \ll \tau_m$. The local ordering and (axial) magnetic frames are implicitly collinear. This yields the following simple spectral density (36):

$$J(\omega) = S^2\tau_m/(1 + \tau_m^2\omega^2) + (1 - S^2)\tau_e'/(1 + \tau_e'^2\omega^2), \qquad [1]$$

where S^2 denotes the square of a generalized order parameter and $1/\tau_e' = 1/\tau_m + 1/\tau_e \approx 1/\tau_e$. When Eq. **1** cannot fit the data, the extended model-free spectral density (28), which allows for a slow local motion associated with S_s^2 and τ_s, and a fast local motion associated with S_f^2 and τ_f, is used. All of the dynamic modes involved are assumed to be decoupled. The form of this spectral density is given by ref. 28:

$$J(\omega) = S_f^2[S_s^2\tau_m/(1 + \omega^2\tau_m^2) + [1 - S_s^2]\tau_s'(1 + \omega^2\tau_s'^2)] + [1 - S_f^2]\tau_f'(1 + \omega^2\tau_f'^2) \qquad [2]$$

Often a reduced form of Eq. **2** is used by setting τ_f to zero. In this case the independent variables in the data-fitting process include S_s^2, τ_s, and S_f^2, with τ_m determined separately as outlined above. We used this form of Eq. **2** as implemented in the program DYNAMICS (37).

1. Slovic AM, Kono H, Lear JD, Saven JG, DeGrado WF (2004) Computational design of water-soluble analogues of the potassium channel KcsA. *Proc Natl Acad Sci USA* 101:1828–1833.
2. Marley J, Lu M, Bracken C (2001) A method for efficient isotopic labeling of recombinant proteins. *J Biomol NMR* 20:71–75.
3. Whitmore L, Wallace BA (2004) DICHROWEB, an online server for protein secondary structure analyses from circular dichroism spectroscopic data. *Nucleic Acids Res* 32:W668–W673.
4. Whitmore L, Wallace BA (2008) Protein secondary structure analyses from circular dichroism spectroscopy: Methods and reference databases. *Biopolymers* 89:392–400.
5. Nietlispach D (2005) Suppression of anti-TROSY lines in a sensitivity enhanced gradient selection TROSY scheme. *J Biomol NMR* 31:161–166.
6. Yang D, Kay LE (1999) Improved 1HN-detected triple resonance TROSY-based experiments. *J Biomol NMR* 13:3–10.
7. Chou JJ, Gaemers S, Howder B, Louis JM, Bax A (2001) A simple apparatus for generating stretched polyacrylamide gels, yielding uniform alignment of proteins and detergent micelles. *J Biomol NMR* 21:377–382.

8. Loria JP, Rance M, Palmer AG (1999) A relaxation-compensated Carr–Purcell–Meiboom–Gill sequence for characterizing chemical exchange by NMR spectroscopy. *J Am Chem Soc* 121:2331–2332.
9. Tollinger M, Skrynnikov NR, Mulder FA, Forman-Kay JD, Kay LE (2001) Slow dynamics in folded and unfolded states of an SH3 domain. *J Am Chem Soc* 123:11341–11352.
10. Delaglio F, *et al.* (1995) NMRPipe: A multidimensional spectral processing system based on UNIX pipes. *J Biomol NMR* 6:277–293.
11. Zimmerman DE, *et al.* (1997) Automated analysis of protein NMR assignments using methods from artificial intelligence. *J Mol Biol* 269:592–610.
12. Goddard TD, Kneller DG (2002) Sparky 3 (University of California, San Francisco).
13. Cornilescu G, Delaglio F, Bax A (1999) Protein backbone angle restraints from searching a database for chemical shift and sequence homology. *J Biomol NMR* 13:289–302.
14. Guntert P (2003) Automated NMR protein structure calculation. *Prog NMR Spectrosc* 43:105–125.
15. Herrmann T, Guntert P, Wuthrich K (2002) Protein NMR structure determination with automated NOE assignment using the new software CANDID and the torsion angle dynamics algorithm DYANA. *J Mol Biol* 319:209–227.
16. Schwieters CD, Kuszewski JJ, Tjandra N, Clore GM (2003) The Xplor-NIH NMR molecular structure determination package. *J Magn Reson* 160:65–73.
17. Koradi R, Billeter M, Wuthrich K (1996) MOLMOL: A program for display and analysis of macromolecular structures. *J Mol Graphics* 14:29–32 and 51–55.
18. Laskowski RA, Rullmannn JA, MacArthur MW, Kaptein R, Thornton JM (1996) AQUA and PROCHECK-NMR: Programs for checking the quality of protein structures solved by NMR. *J Biomol NMR* 8:477–486.
19. Koenig SH (1975) Brownian motion of an ellipsoid. A correction of Perrin's results. *Biopolymers* 14:2421–2423.
20. Perrin F (1934) Mouvement Brownien d'um ellipsoide (I). Dispersion dielectrique pour des molecules ellipsoidales. *J Phys Radium* 5:497–511.
21. Georgieva D, *et al.* (2004) Oligomerization of the proteolytic products is an intrinsic property of prion proteins. *Biochem Biophys Res Commun* 323:1278–1286.
22. Georgieva D, *et al.* (2005) Conformational states of the *Rapana thomasiana* hemocyanin and its substructures studied by dynamic light scattering and time-resolved fluorescence spectroscopy. *Biophys J* 88:1276–1282.
23. Georgieva DN, Genov N, Hristov K, Dierks K, Betzel C (2004) Interactions of the neurotoxin vipoxin in solution studied by dynamic light scattering. *Biophys J* 86:461–466.
24. Kaszynska K, *et al.* (2002) Dynamic light scattering and NMR studies of napin. *J Sol Chem* 31:987–993.
25. Chill JH, Louis JM, Delaglio F, Bax A (2007) Local and global structure of the monomeric subunit of the potassium channel KcsA probed by NMR. *Biochim Biophys Acta* 1768:3260–3270.
26. Lefevre JF, Dayie KT, Peng JW, Wagner G (1996) Internal mobility in the partially folded DNA binding and dimerization domains of GAL4: NMR analysis of the N-H spectral density functions. *Biochemistry* 35:2674–2686.
27. Farrow NA, Zhang O, Szabo A, Torchia DA, Kay LE (1995) Spectral density function mapping using 15N relaxation data exclusively. *J Biomol NMR* 6:153–162.
28. Clore GM, *et al.* (1990) Deviations from the simple two-parameter model-free approach to the interpretation of nitrogen-15 nuclear magnetic relaxation of proteins. *J Am Chem Soc* 112:4989–4991.
29. Chill JH, Louis JM, Baber JL, Bax A (2006) Measurement of 15N relaxation in the detergent-solubilized tetrameric KcsA potassium channel. *J Biomol NMR* 36:123–136.
30. Palmer AG, III (2001) NMR probes of molecular dynamics: Overview and comparison with other techniques. *Annu Rev Biophys Biomol Struct* 30:129–155.
31. Tjandra N, Wingfield P, Stahl S, Bax A (1996) Anisotropic rotational diffusion of perdeuterated HIV protease from ^{15}N NMR relaxation measurements at two magnetic fields. *J Biomol NMR* 8:273–284.
32. Kay LE, Torchia DA, Bax A (1989) Backbone dynamics of proteins as studied by 15N inverse detected heteronuclear NMR spectroscopy: Application to staphylococcal nuclease. *Biochemistry* 28:8972–8979.
33. Krizova H, Zidek L, Stone MJ, Novotny MV, Sklenar V (2004) Temperature-dependent spectral density analysis applied to monitoring backbone dynamics of major urinary protein-I complexed with the pheromone 2- sec-butyl-4,5-dihydrothiazole. *J Biomol NMR* 28:369–384.
34. Palmer AG, III, Massi F (2006) Characterization of the dynamics of biomacromolecules using rotating-frame spin relaxation NMR spectroscopy. *Chem Rev* 106:1700–1719.
35. Lee AL, Sharp KA, Kranz JK, Song XJ, Wand AJ (2002) Temperature dependence of the internal dynamics of a calmodulin-peptide complex. *Biochemistry* 41:13814–13825.
36. Lipari G, Szabo A (1982) Model-free approach to the interpretation of nuclear magnetic resonance relaxation in macromolecules. 1. Theory and range of validity. *J Am Chem Soc* 104:4546–4559.
37. Fushman D, Cahill S, Cowburn D (1997) The main-chain dynamics of the dynamin pleckstrin homology (PH) domain in solution: Analysis of 15N relaxation with monomer/dimer equilibration. *J Mol Biol* 266:173–194.
38. Smart OS, Neduvelil JG, Wang X, Wallace BA, Sansom MS (1996) HOLE: A program for the analysis of the pore dimensions of ion channel structural models. *J Mol Graphics* 14: 354–360, 376.

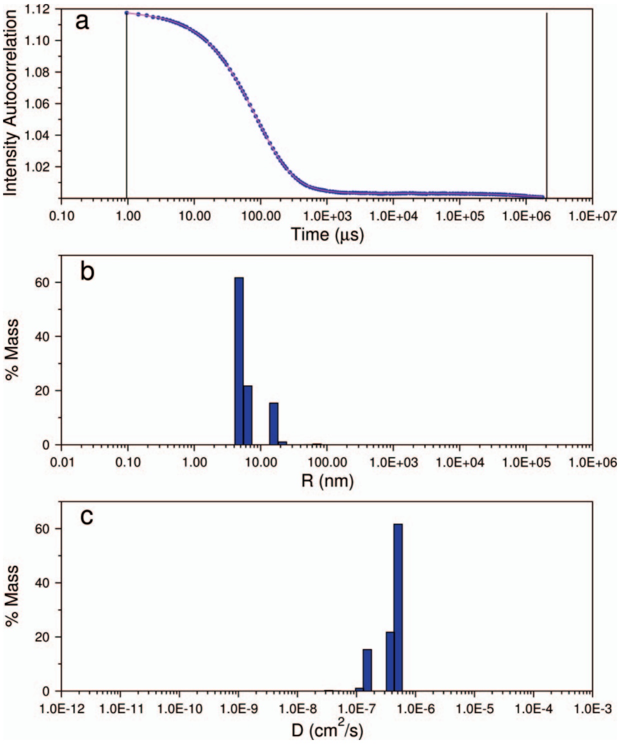

Fig. S1. Dynamic light scattering of WSK3. (*a*) Autocorrelation of the scattering intensity (blue dots) as a function of time. The magenta curve is the theoretical fitting using regularization analysis. (*b* and *c*) The resulting size distribution is plotted as a function of hydrodynamic radius (*b*) and diffusion coefficient (*c*). In this particular sample, 84% of the mass is associated with $R \approx 47$–62 Å (weighted average = 52 Å), in excellent agreement with the NMR diffusion measurements of the tetramer population. The minor population with hydrodynamic radius of ≈150 Å is probably from loosely associated trimers (or higher oligomers) of the tetramers.

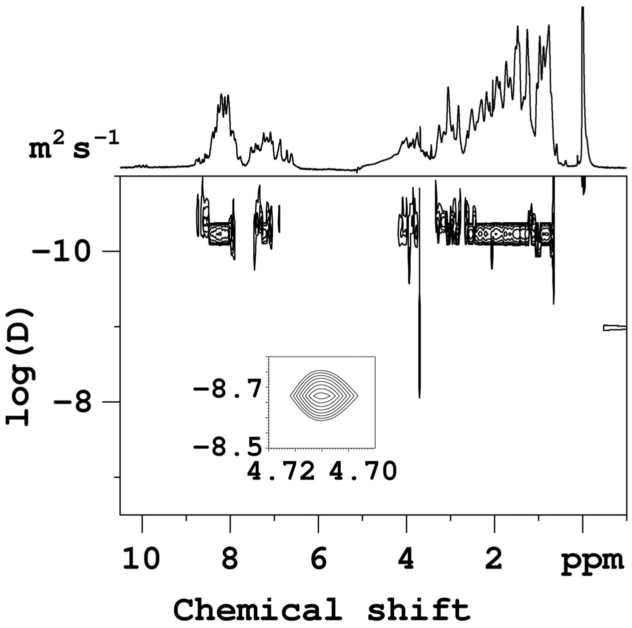

Fig. S2. Determination of oligomerization state of WSK3 in water by NMR diffusion measurements. Two-dimensional diffusion-weighted DOSY spectra of WSK3 were acquired at 30 °C with water suppression. A 1D reference spectrum is shown on the top. The *Inset* shows the diffusion of water in the same sample and under the same experimental conditions but without water suppression. The vertical axis is the diffusion coefficient, D, on a logarithmic scale.

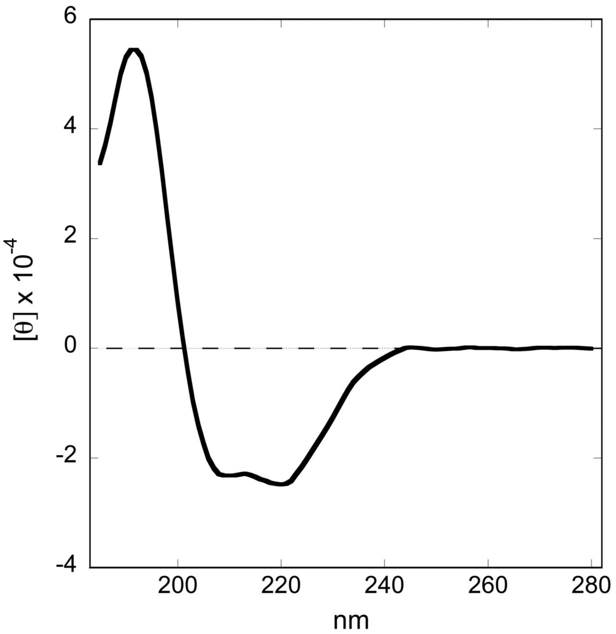

Fig. S3. CD spectrum of WSK3. An α-helical content of ≈75–80% was estimated by using the CDSSTR algorithm. This is similar to the 70% helical content estimated by NMR analysis.

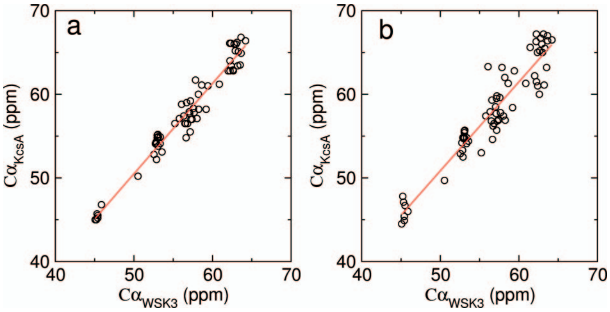

Fig. S4. Comparison of C_α chemical shifts of unmutated residues in WSK3 at pH 4.5 with those of the corresponding residues in KcsA monomer at pH 4.2 (*a*) and KcsA tetramer at pH 6.0 (*b*). The KcsA chemical shift data were taken from BMRB Entry No. 7428 and No. 15853. The red lines are linear regression of the data, yielding a correlation coefficient of 0.98 and 0.95, and slopes of 1.08 ± 0.03 and 1.06 ± 0.05 in *A* and *B*, respectively.

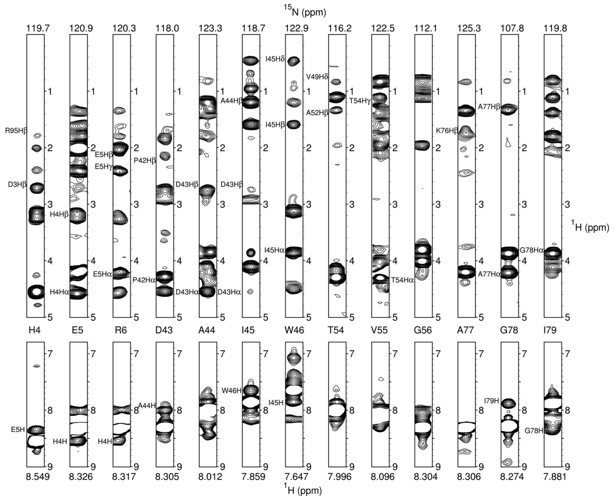

Fig. S5. Examples of 3D NOE connectivity from different regions in WSK3. (*A*) ^{15}N-edited 3D NOESY strip plots for residues in the outer helix (H4, E5, R6), pore helix (D43, A44, I45, W46), selectivity filter (T54, V55, G56), and inner helix (A77, G78, I79). Several interresidue NOE cross-peaks are labeled to the left of the strips, whereas the intraresidue cross-peaks are not labeled. The spectral region from 5 to 6.8 ppm is excluded. The amide ^{15}N chemical shift for each slice is indicated on the top of the strips, and the amide proton chemical shift is indicated at the bottom of each slice.

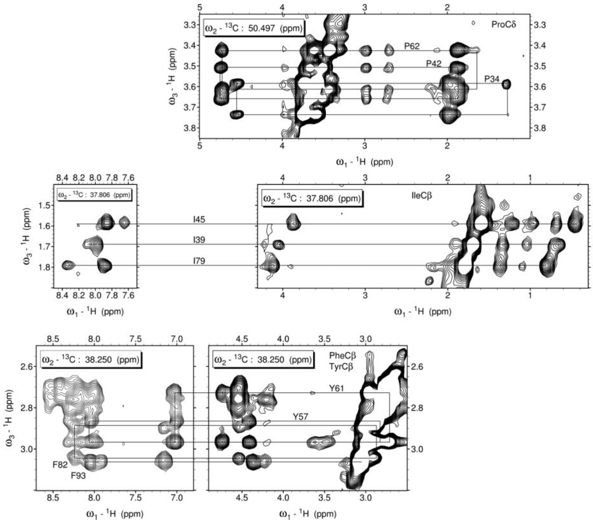

Fig. S5 *continued*. (*B*) ^{13}C-edited 3D NOESY slices at the Pro Cδ, Ile Cβ, and Phe/Tyr Cβ regions. The assigned NOE cross-peaks of P34, P42, P62, I39, I45, I79, F82, F93, Y57, and Y61 are indicated by connecting lines. The spin pairs associated with these and other NOE cross-peaks and the number of intra-subunit distance restraints for individual residues are summarized in Figs. S6c and S7.

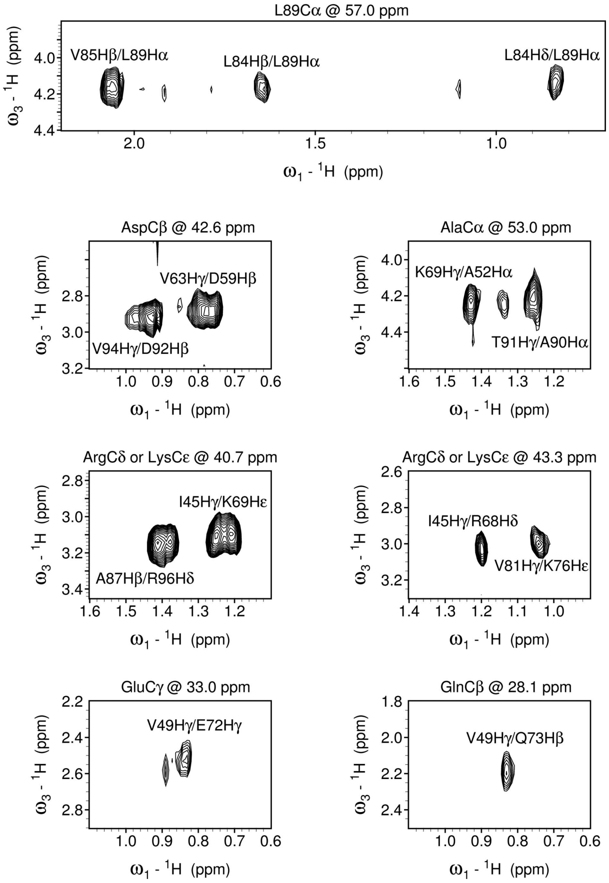

Fig. S5 ***continued.*** (*C*) Several representative slices from ^{13}C-edited and ^{13}C- and ^{15}N-filtered 3D NOESY collected on a 1:1 mixture of unlabeled protein and ^{13}C and ^{15}N uniform labeled protein. Slices depicting L89 Cα at 57.0 ppm, Asp Cβ at 42.6 ppm, Ala Cα at 53.0 ppm, Arg Cδ or Lys Cε at 40.7 ppm and 43.3 ppm, Glu Cγ at 33.0 ppm, and Gln Cβ at 28.1 ppm are shown. These are intersubunit NOE cross-peaks as labeled.

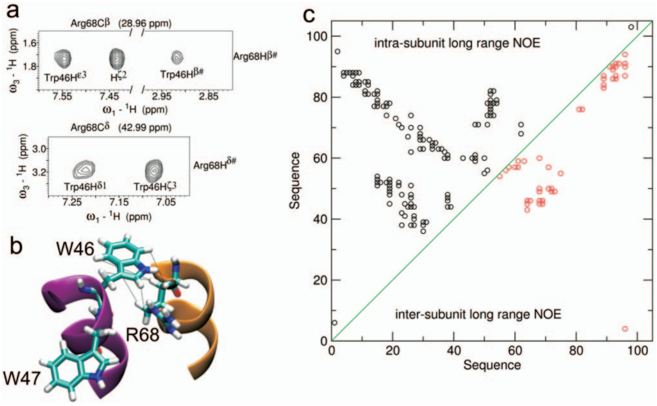

Fig. S6. Long-range intra- and intersubunit NOE connectivity was determined by using heteronuclear isotope-edited and isotope-filtered 3D NOESY experiments with uniformly $^{13}C/^{15}N$-labeled samples and with 1:1 mixtures of $^{13}C/^{15}N$-labeled and unlabeled samples. (*a*) Examples of intersubunit NOE cross-peaks between W46 and R68. (*b*) Corresponding distance restraints depicted on the determined structures (only two adjacent subunits in the tetramer are shown). (*c*) Connectivity plot summarizing intrasubunit long-range NOEs (black) and intersubunit long-range NOEs (red). Note that each point in *C* can represent more than one NOE cross-peak. For example, the red point at the crossing between W46 and R68 represents 5 NOE restraints shown in *a* and *b*. It should also be noted that whereas all arginine backbone resonances in WSK3 are unambiguously assigned, the arginine side-chain peaks are overlapped. The ambiguity in the assignment of the peaks shown in *a* and *b* was reduced in the iterative structure calculation, in which additional intersubunit NOE cross-peaks, including D43-T64, I45-T64, and I45-K69, have been unambiguously assigned in the intersubunit filtered NOESY.

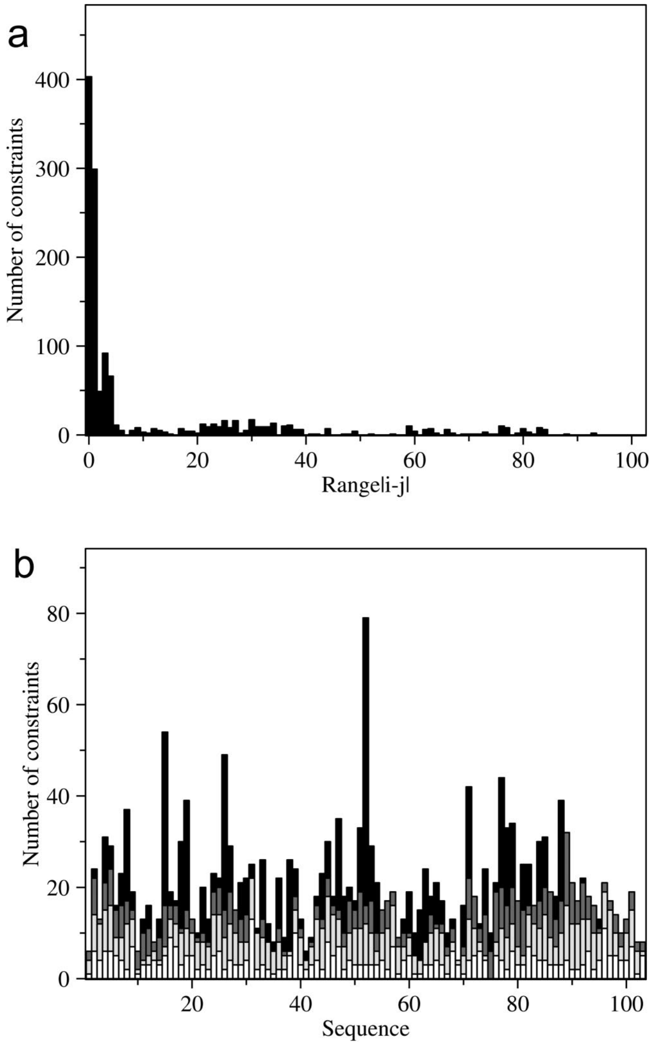

Fig. S7. Total number of intrasubunit distance restraints is plotted based on distance range (*a*) and individual residues (*b*). In *b*, intraresidual, short-range, medium-range, and long-range constraints are marked with white, light gray, dark gray, and solid black bars, respectively. The intersubunit long-range NOEs are depicted in Fig. S6 and are not included in this figure.

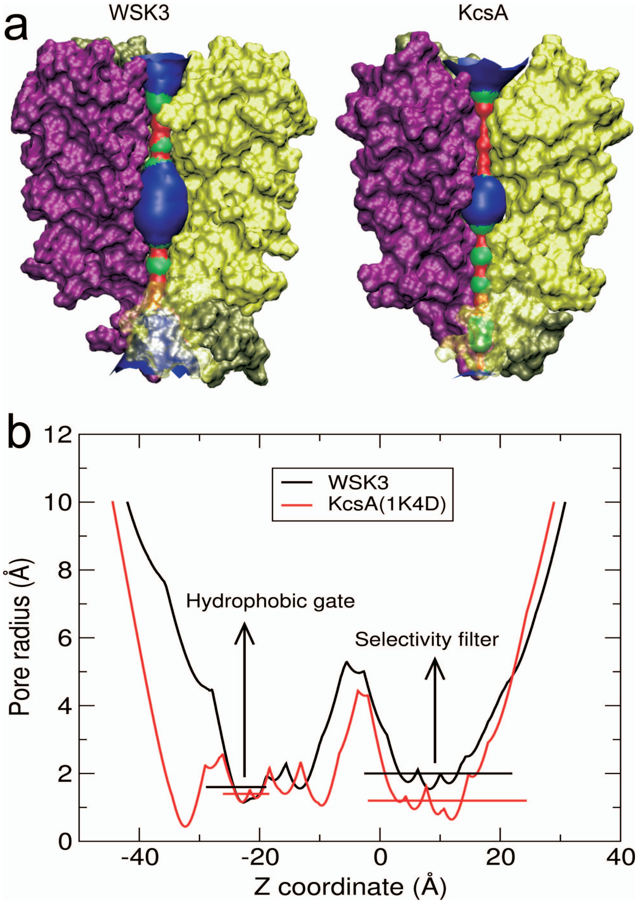

Fig. S8. Comparison of the pore profiles between WSK3 and KcsA (PDB ID code 1K4D). (*a*) Surface rendering of the channel and pore profile. The program HOLE (38) was used to generate the profiles. WSK3 and KcsA are shown in surface rendering, with the front subunit removed for display clarity. The pore radius is classified into categories of small (red), medium (green), and large (blue). (*b*) Plot of pore radius as a function of the ''*z*'' coordinate along the pore axis for WSK3 (black) and KcsA (red). Notice that both intracellular entrance ($z \approx 1$–30 Å) and the selectivity filter ($z \approx 10$ Å) have a significantly larger radius in WSK3 than in KcsA. A larger selectivity filter radius might render the filter impermeable to K^+.

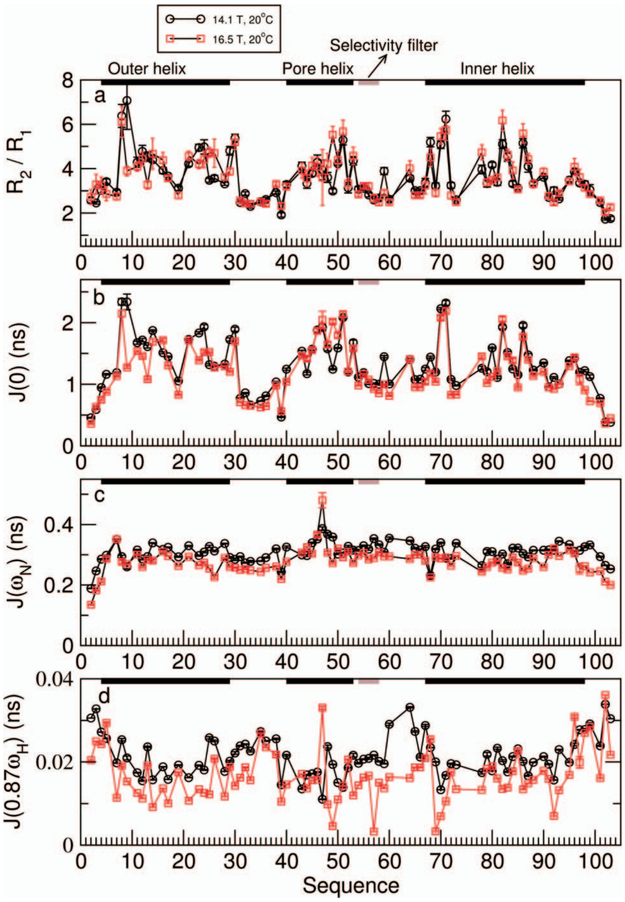

Fig. S9. Qualitative analysis of WSK3 dynamics. Backbone ^{15}N R_2/R_1 ratio and the reduced spectral density function values $J(0)$, $J(\omega_N)$, and $J(0.87\omega_H)$ are calculated from the dynamics data shown in Fig. 4 *a–c*. The relaxation data were acquired at 20 °C and at 14.1 T (circles) and 16.5 T (squares).

Table S1. NMR and refinement statistics for WSK3 tetramer structures

NMR distance and dihedral restraints	WSK3 tetramer		
Distance restraints per subunit			
Total NOE	1321		
Intraresidue	403		
Interresidue	849		
Sequential ($\|i-j\|=1$)	299		
Medium-range ($\|i-j\|\leq 4$)	204		
Long-range ($\|i-j\|>4$)	346		
Intersubunit	69		
Hydrogen bonds	48		
Total dihedral angle restraints	92		
ϕ	46		
ψ	46		
RDC restraints	41[*]		
Structure Statistics	With RDC		Without RDC
Violations (mean and SD)	Harmonic potential	Half-harmonic (square) potential	
Distance restraints, Å	0.041 ± 0.002	0.050 ± 0.003	0.031 ± 0.002
Dihedral angle restraints, °	0.747 ± 0.148	0.743 ± 0.141	0.475 ± 0.063
RDC restraints, Hz	0.681 ± 0.050	0.781 ± 0.050	
Max. dihedral angle violation, °	4.780	4.830	4.140
Max. distance restraint violation, Å	0.430	0.820	0.430
Max. RDC restraints, Hz	2.920	2.710	
Deviations from idealized geometry			
Bond lengths, Å	0.004 ± 0.000	0.004 ± 0.000	0.003 ± 0.000
Bond angles, °	0.526 ± 0.012	0.529 ± 0.014	0.487 ± 0.006
Impropers, °	0.432 ± 0.014	0.424 ± 0.010	0.325 ± 0.007
Average pairwise r.m.s.d.[†], Å			
Heavy	1.86 ± 0.14[‡]	1.88 ± 0.14[‡]	1.60 ± 0.11[‡]
	2.51 ± 0.20[§]	2.46 ± 0.18[§]	2.17 ± 0.12[§]
Backbone	1.15 ± 0.16[‡]	1.20 ± 0.16[‡]	0.87 ± 0.11[‡]
	1.80 ± 0.25[§]	1.75 ± 0.19[§]	1.41 ± 0.14[§]

[*] RDCs for $^{1}H_{N}$-^{15}N.

[†] Pairwise r.m.s.d. was calculated among the 20 refined structures.

[‡] Calculated over the helical regions of the tetramers (4–30, 44–53, 69–96).

[§] Calculated over the entire sequence of the tetramers.

Table S2. Intersubunit long-range NOE constraints and related salt bridges identified in the WSK3 structures

NOE distance restraints	Intersubunit salt bridge observed
Assign (segid a and resid 60 and name HE) (segid b and resid 68 and name HE) 6.0 4.2 0.5	ASP59 chain A ARG68 chain B ASP59 chain B ARG68 chain C ASP59 chain C ARG68 chain D ASP59 chain D ARG68 chain A
Assign (segid a and resid 81 and name HG1#) (segid a and resid 12 and name HN) 4.0 2.2 0.5	GLU12 chain A LYS76 chain B
Assign (segid a and resid 12 and name HG#) (segid a and resid 85 and name HN) 6.0 4.2 0.5	GLU12 chain B LYS76 chain C
Assign (segid a and resid 84 and name HD2#) (segid a and resid 12 and name HN) 6.0 4.2 0.5	GLU12 chain C LYS76 chain D
These 3 are intrasubunit long-range NOE, but they help to form the intersubunit salt bridge between side chain of E12 and K76.	GLU12 chain D LYS76 chain A
Assign (segid a and resid 50 and name HG#) (segid b and resid 68 and name HG#) 6.0 4.2 0.5	GLU50 chain A ARG68 chain B
Assign (segid a and resid 49 and name HB) (segid b and resid 68 and name HE) 6.0 4.2 0.5	GLU50 chain C ARG68 chain D
Assign (segid a and resid 46 and name HZ3) (segid b and resid 68 and name HD#) 6.0 4.2 0.5	GLU50 chain D ARG68 chain A

Table S3. Intrasubunit NOE constraints and related salt bridges identified in the WSK3 structures

NOE distance restraints	Intrasubunit salt bridge observed
Assign (segid a and resid 60 and name HD#) (segid a and resid 43 and name HB2) 5.0 3.2 0.5	ASP43 chain A ARG60 chain A
Assign (segid a and resid 60 and name HD#) (segid a and resid 43 and name HB1) 6.0 4.2 0.5	ASP43 chain B ARG60 chain B
	ASP43 chain C ARG60 chain C
	ASP43 chain D ARG60 chain D
Assign (segid a and resid 59 and name HA) (segid a and resid 60 and name HN) 5.0 3.2 0.5	ASP59 chain A ARG60 chain A
Assign (segid a and resid 59 and name HB#) (segid a and resid 60 and name HN) 4.0 2.2 0.5	ASP59 chain B ARG60 chain B
	ASP59 chain D ARG60 chain D
Assign (segid a and resid 92 and name HA) (segid a and resid 93 and name HN) 5.0 3.2 0.5	ASP92 chain A ARG95 chain A
Assign (segid a and resid 92 and name HA) (segid a and resid 94 and name HN) 5.0 3.2 0.5	ASP92 chain B ARG95 chain B
	ASP92 chain C ARG95 chain C
	ASP92 chain D ARG95 chain D
Assign (segid a and resid 14 and name HA) (segid a and resid 17 and name HN) 5.0 3.2 0.5	GLU14 chain A LYS17 chain A
	GLU14 chain B LYS17 chain B
	GLU14 chain C LYS17 chain C
Assign (segid a and resid 28 and name HB#) (segid a and resid 24 and name HE#) 5.0 3.2 0.5	GLU28 chain A LYS24 chain A
Assign (segid a and resid 28 and name HB#) (segid a and resid 24 and name HG#) 5.0 3.2 0.5	GLU28 chain B LYS24 chain B
	GLU28 chain C LYS24 chain C
Assign (segid a and resid 2 and name HB#) (segid a and resid 95 and name HE) 5.0 3.2 0.5	GLU5 chain A ARG95 chain A
Assign (segid a and resid 97 and name HA) (segid a and resid 100 and name HB#) 4.0 2.2 0.5	GLU97 chain B ARG100 chain B
	GLU97 chain D ARG100 chain D
Assign (segid a and resid 101 and name HN) (segid a and resid 97 and name HA) 5.0 3.2 0.5	GLU97 chain D ARG101 chain D

Table S4. Comparison of experimental and best-fitting dynamics data between WSK3 and the cytoplasmic region of KcsA

	$\langle J(0)\rangle$	$\langle J(\omega_N)\rangle$	$\langle J(0.87\omega_H)\rangle$	$\langle S^2\rangle$	$\langle \tau_s\rangle$, ns
WSK3	1.5	0.3	0.02	0.17	0.7
Cytoplasmic KcsA region*	5.0	0.25	0.015	0.3	1.2

* The KcsA data are taken from figure 5 and table 1 of ref. 29.